Journal of Materials Chemistry A

ROYAL SOCIETY OF CHEMISTRY

PAPER

Cite this: *J. Mater. Chem. A*, 2021, **9**, 1720

Experimental considerations to study Li-excess disordered rock salt cathode materials†

Hyeseung Chung,[a] Zachary Lebens-Higgins,[b] Baharak Sayahpour,[a] Carlos Mejia,[a] Antonin Grenier,[c] Gabrielle E. Kamm,[c] Yixuan Li,[a] Ricky Huang,[a] Louis F. J. Piper,[b] Karena W. Chapman,[c] Jean-Marie Doux *[a] and Ying Shirley Meng *[a]

Cation-disordered rock salt materials have attracted much interest as high energy density cathode materials due to their anionic electrochemical activity, providing them extra capacity, along with their lower cost. They are, however, still the subject of numerous studies as they suffer from poor cyclability and relatively slow kinetics compared to traditional intercalation materials. In this work, several important experimental considerations, that must be taken into account when studying Li-excess cation disordered rock salt cathode materials, are introduced. First, the key synthesis parameters were identified to enable a lower-temperature, morphology-controlled synthesis of the Li_3NbO_4-based disordered rock salt cathodes $Li_{1.3}TM_{0.4}Nb_{0.3}O_2$ (TM = Fe, Mn), using nano-sized precursors. After evaluating the influence of the morphology on the cyclability of the electrode, two key challenges that hinder the practical implementation of these systems are revealed – ambient air-induced surface contamination and electrolyte compatibility. Thermal gravimetric analysis and X-ray diffraction on the nano-sized cathodes confirmed that prolonged air exposure generates a large amount of surface species, responsible for the large decrease in the first discharge capacity. Moreover, the influence of the electrolyte on the evolution of the cathode–electrolyte interphase was investigated using X-ray photoelectron spectroscopy. The results show that cation-disordered rock salt cathodes go through significant Li-salt degradation and develop thick cathode–electrolyte interphase with the electrolytes compatible with Li-excess layered cathode materials $Li[Li_{0.144}Ni_{0.136}Co_{0.136}Mn_{0.544}]O_2$, highlighting the importance of evaluating and finding compatible battery chemistries.

Received 10th August 2020
Accepted 15th December 2020

DOI: 10.1039/d0ta07836k

rsc.li/materials-a

Introduction

The ever-growing demand in energy storage has a large impact on the research of high capacity electrode materials for Li-ion batteries. In previous decades, lithium-excess transition metal (TM) oxides have attracted attention, both in academia and industry, as one of the most promising next-generation cathode materials.[1,2] This class of materials pushes the limits of the TM redox storage capacity by additionally activating the anionic redox of the lattice oxygen. Recently, several groups introduced a new paradigm with the cation-disordered rock salt (DRS) structured cathode materials.[3–5] These materials were previously believed not to be electrochemically active as the random distribution of the cations in the cell prevents the formation of distinct Li diffusion pathways required for cycling.[6] However, computational and experimental studies confirmed that a percolation network of 0-TM channels develops when the Li content exceeds ≈1.09, leading to a reversible capacity as in traditional intercalation cathode materials.[7] This discovery, by changing the design principles of cathode materials, vastly expanded the chemical space of possible cathodes. Over the last few years, several Li-excess DRS cathode materials were synthesized, developed, and characterized to evaluate their potential as the next generation of cathode materials.[4,8–10]

Despite the growing interest in DRS cathode materials, there are still limited studies of their synthesis mechanisms and how the synthesis conditions affect their morphology and electrochemical performances. As one of the most studied classes of DRS materials, TM-substituted Li_3NbO_4 exhibits high discharge capacities – around 300 mA h g^{-1} at 60 °C.[3] These materials are usually prepared by either high-temperature solid-state synthesis or mechanochemical synthesis, starting from TM oxide precursors and a Li-source, such as Li_2CO_3 or Li_2O. Nevertheless, the solid-state synthesis method comes with its own disadvantages. For instance, its long dwelling at high

[a]Department of Nanoengineering, University of California San Diego, La Jolla, California 92093, USA. E-mail: shirleymeng@ucsd.edu; jdoux@ucsd.edu

[b]Department of Physics, Applied Physics and Astronomy, Binghamton University, Binghamton, New York 13902, USA

[c]Department of Chemistry, Stony Brook University, Stony Brook, New York 11794, USA

† Electronic supplementary information (ESI) available. See DOI: 10.1039/d0ta07836k

temperature leads to Li evaporation and particle agglomeration.[10–12] The mechanochemical synthesis process, which involves high energy ball-milling of the reagents without heat-treatment, allows for the obtention of smaller particles compared to those obtained through the solid-state methods.[4,13–15] Unfortunately, it also generates defects and/or amorphous species during synthesis, making the characterization of the product extremely challenging. Additionally, the long high energy ball milling step often generates impurities coming from the grinding media, such as ZrO_2 or WC.[13] As a result, both of these methods are not adequate to characterize the effect of particle morphology on the kinetic limitations of DRS materials.[3]

Herein, we conducted a comprehensive study of the synthesis of Li_3NbO_4-based cathode materials and analyzed various parameters of the solid-state reaction that can affect both the transition metal segregation and the particle morphology. Using nano-sized precursors, we have successfully produced phase-pure DRS material at reduced temperature, while controlling the particle morphology. The electrochemical performances were then evaluated and compared with those of micron-sized materials reported in literature.

Based on this study, the cycling stability of these materials, although improved, is still limited compared with other anionic redox cathodes, such as Li-excess layered materials. Thus, we have identified two important challenges that hinder the practical implementation of DRS cathode materials. First, we have investigated how ambient air exposure can lead to the formation of surface species using X-ray diffraction (XRD), thermogravimetric analysis (TGA), and X-ray photoelectron spectroscopy (XPS). We then proposed a heat-treatment process to partially reverse the contamination of the air-exposed samples. Finally, we have investigated the electrolyte compatibility by testing DRS materials with two other advanced electrolytes, commonly used in the literature for Li-excess layered material.[17,18] Even compared with other high-voltage cathode materials, the improper choice of electrolyte for a DRS material has a drastic effect associated with the formation of an excessive cathode–electrolyte interphase (CEI) layer. The study of these two main factors aims at providing guidelines to the scientific community when evaluating the practical performances of DRS cathode materials.

Experimental methods

Synthesis of materials

Li_3NbO_4, $Li_{1.3}Fe_{0.4}Nb_{0.3}O_2$, and $Li_{1.3}Mn_{0.4}Nb_{0.3}O_2$ were synthesized by solid-state reaction using two different sized metal oxide precursors. Nano-sized metal oxide precursors were used for nanoparticle cathode synthesis, whereas micron-sized metal oxide precursors were used for non-morphology-controlled cathode synthesis.

Nano-sized Nb_2O_5 precursor (n-Nb_2O_5) was synthesized *via* solvothermal method. 0.5 g of $NbCl_5$ (Alfa Aesar, >99.9%) was added to 50 mL of anhydrous benzyl alcohol (Sigma-Aldrich, >99.8%) while continuously stirring. The mixture was transferred into a 100 mL Teflon cup, slid into a stainless-steel autoclave, and carefully sealed in an Ar-filled glovebox (MBraun, Germany). The autoclave was heated in a furnace at 240 °C for 31 hours. The resulting solution was centrifuged to separate the white Nb_2O_5 product. The product was repeatedly washed with ethanol and finally dried in vacuum at 60 °C.

Nano-sized Mn_2O_3 precursor (n-Mn_2O_3) was prepared by polyol method. In this set up, 0.02 mol of $Mn(CH_3COO)_2 \cdot 4H_2O$ (Acros, >99%) and 0.02 mol of citric acid (Sigma-Aldrich, >99.5%) were added to 100 mL of diethylene glycol (Sigma, >99%) in a 250 mL round bottom flask connected to a reflux. The mixture was continuously stirred while it was heated to 220 °C for 2 h and cooled back down to room temperature. Through this solution reaction, a light brown coloured precipitate was harvested. The precipitate was washed with ethanol several times *via* centrifugation–redispersion cycles to remove any possible residual reactants. Afterward, the precipitate was heated at 450 °C for 12 h, manually mixed with an agate mortar and pestle, and then heated again at 600 °C for 2 h to obtain the final product. All the reactions and heat-treatments were conducted in air. Nano-sized Fe_2O_3 (n-Fe_2O_3) has been purchased (Aldrich, nanopowder) and used without further treatment. XRD and SEM of all metal oxide precursors are shown in Fig. S1 and S2.†

For Li_3NbO_4 nanoparticle preparation, stoichiometric amounts of $LiOH \cdot H_2O$ (Sigma-Aldrich, >98%) and n-Nb_2O_5 were manually mixed in an agate mortar and pestle for 15 min. The mixed powder was then pelletized, put into a quartz tube, and heated at 700 °C for 1 h in air. The pellet in the quartz tube was then quenched in a dry ice/isopropanol bath.

$Li_{1.3}Fe_{0.4}Nb_{0.3}O_2$ and $Li_{1.3}Mn_{0.4}Nb_{0.3}O_2$ nanoparticles were prepared from stoichiometric amounts of Li_2CO_3 (Sigma-Aldrich, >99%), n-Nb_2O_5, and n-Fe_2O_3 or n-Mn_2O_3 respectively. These precursors were first thoroughly mixed by wet mechanical ball milling (Retsch PM 100) at 400 rpm for 2 h. A zirconia jar and 5 mm-diameter yttria-stabilized zirconia balls were used with isopropanol solvent. The obtained product was dried in air and pressed into a pellet before heat-treatment. In a typical synthesis, $Li_{1.3}Fe_{0.4}Nb_{0.3}O_2$ was calcined at 750 °C for 5 h in air, and $Li_{1.3}Mn_{0.4}Nb_{0.3}O_2$ was calcined at 750 °C for 5 h in Ar in a tube furnace. During the study of the effect of the temperature, a 10% excess of Li_2CO_3 was added for the samples when high temperature heat treatments were performed (950 °C and 1050 °C) in order to compensate for Li evaporation.

Non-morphology controlled Li_3NbO_4, $Li_{1.3}Fe_{0.4}Nb_{0.3}O_2$, and $Li_{1.3}Mn_{0.4}Nb_{0.3}O_2$ were prepared from Li_2CO_3 and micron-sized metal oxide precursors – Nb_2O_5 (Alfa Aesar, >99.9985%) and Fe_2O_3 (Strem, >99.995%) or Mn_2O_3 (Strem, >99%). Li_3NbO_4 was prepared similarly to previous reports.[3] For $Li_{1.3}Fe_{0.4}Nb_{0.3}O_2$ and $Li_{1.3}Mn_{0.4}Nb_{0.3}O_2$, Li_2CO_3, Nb_2O_5, and Fe_2O_3 or Mn_2O_3 were mixed by wet mechanical ball milling at 400 rpm for 2 h in a zirconia jar using 5 mm-diameter yttria-stabilized zirconia balls and isopropanol solvent. The obtained products were also dried and pelletized before heat-treatment. In a typical synthesis, non-morphology controlled $Li_{1.3}Fe_{0.4}Nb_{0.3}O_2$ and $Li_{1.3}Mn_{0.4}Nb_{0.3}O_2$ were heat-treated for 24 h at 950 °C in air (for Fe sample) or in Ar (for Mn sample). Here again, a 10% excess of Li_2CO_3 was added for 950 °C and 1050 °C heat-treatments to

compensate for Li evaporation at high temperatures, while a stoichiometric amount was used for lower temperatures. All the disordered rock salt cathode materials in this study were stored in an Ar-filled glovebox before use.

Li-excess NMC ($Li[Li_{0.144}Ni_{0.136}Co_{0.136}Mn_{0.544}]O_2$), used for the electrolyte study, was synthesized as in a previous study.[19]

Material characterization

The crystal structures were characterized by X-ray diffraction (XRD) using Cu Kα ($\lambda = 1.54059$ Å) or Mo Kα ($\lambda = 0.71073$ Å) radiations. For Cu Kα radiation, a Bruker D8 diffractometer was used, and the data was collected by continuous scanning of a detector covering an angular range from 10.0° to 80.0°. A Bruker APEX II Ultra diffractometer was used for Mo Kα radiation. The diffraction images gathered by the 2D detector were merged and integrated in DIFFRAC.EVA (Bruker, 2018) to produce 2d-plots. All Rietveld refinements were conducted using a pseudo-Voigt profile in FullProf software.[20] Zeiss Sigma 500 or FEI Apreo scanning electron microscope (SEM) with energy dispersive X-ray spectroscopy (EDS) was used to characterize the particle morphology and the elemental distribution. Thermogravimetric analysis (TGA) experiments were performed using a PerkinElmer Simultaneous Thermal Analyzer (STA) 6000. The sample was placed on a ceramic pan under a continuous 20 mL min^{-1} N_2 gas flow during the measurement. The testing procedure consisted of ramping up the temperature at a rate of 5 °C min^{-1}, with isothermal dwell time of 1 hour at 150 °C, 350 °C, and 500 °C. X-ray photoelectron spectroscopy (XPS) was performed using a Kratos Axis Supra spectrometer with an Al anode source operated at 15 kV. For surface contamination study, all the spectra were calibrated to Nb 3d peak associated with Nb^{5+} at 207.1 eV. O 1s core region was scaled with lattice O peak at 530.2 eV. C 1s core region was scaled according to the nearby Nb 3d peak area.

For the Li-rich NMC and pristine Mn-DRS samples in the electrolyte compatibility study, the C–C peak associated with carbon black was aligned to 284.8 eV for energy calibration. Due to differential charging effects for the Mn-DRS samples (see Fig. S11† on carbon black/PVDF), the Nb 3d peak associated with Nb^{5+} was aligned to 207.1 eV to identify changes relative to the active material. The compositional analysis was determined based on the relative sensitivity factors of the Li 1s, P 2p, F 1s, and O 1s. The Li 1s has a very low sensitivity factor and can strongly depends on the choice of background. As such, the Li 1s is included in the compositional analysis in Fig. 6 mainly to highlight the large variation in lithium at the CEI observed with different electrolytes for Li-rich NMC and Mn-DRS. The thickness calculation was based on approximating the cathode particles as a spherical system with a uniform CEI overlayer, following other CEI studies,[21–23] and using the model given by Baer *et al.*[24] For simplicity, the thickness was based on the relative intensity of O 1s CEI components *versus* the O 1s TM–O lattice peak. All spectra were normalized based on the closest active material peak in binding energy so that collected photoelectrons were from a similar probing depth. The F 1s (687 eV) was scaled by the Mn 2p (640 eV), the O 1s was scaled by the lattice oxygen peak, and the P 2p (135 eV) and Li 1s (56 eV) were scaled by the Mn 3p (50 eV). A table of peak positions for CEI components are detailed in Table S1.†

Electrochemical characterization

The summary of the electrochemical testing conditions used in this study, including details on the coin cell fabrication, is listed in Tables S2 and S3.† To fabricate $Li_{1.3}Fe_{0.4}Nb_{0.3}O_2$ and $Li_{1.3}Mn_{0.4}Nb_{0.3}O_2$ cathode electrodes, the powder of active material and carbon black were first mixed in 4 : 1 weight ratio using a planetary ball mill (Retsch PM 100) for 2 h at 300 rpm, in a zirconia jar with 3 mm-diameter yttria-stabilized zirconia balls. Polyvinylidene fluoride (PVDF) was then added to the mixture in a Thinky mixer vial, such that the composite consists of 72 wt% active materials, 18 wt% carbon black, and 10 wt% PVDF. After adding *N*-methyl pyrrolidone (NMP) to the mixture, the slurry was made by mechanical mixing in a Thinky mixer. The slurry was casted on an aluminium foil used as current collector and dried at 80 °C in vacuum overnight. As-prepared electrodes were punched, uniaxially pressed at about 180 MPa, and then stored in an Ar-filled glovebox before cell assembly.

For electrochemical characterization, lithium metal was used as the negative (counter) electrode. The baseline electrolyte was a 1 M solution of lithium hexafluorophosphate ($LiPF_6$) in a 3 : 7 volume mixture of ethylene carbonate (EC) and dimethyl carbonate (DMC). For the electrolyte compatibility study, two additional electrolytes were prepared: (i) 1 M of lithium hexafluorophosphate ($LiPF_6$) in a 3 : 7 volume mixture of ethylene carbonate (EC) and dimethyl carbonate (DMC) with 2 wt% lithium difluoro(oxalate)borate (LiDFOB) as an additive (denoted as LiDFOB electrolyte), and (ii) 1 M $LiPF_6$ in a 1 : 4 volume mixture of fluoroethylene carbonate (FEC) and dimethyl carbonate (DMC) (denoted as FEC electrolyte). The moisture contents of the three electrolytes were verified using a Coulometric Karl Fisher Titrator and were in the range of 10–15 ppm.

All the cells used for the electrochemical tests were assembled using R2032-type coin cells in an Ar-filled glovebox. n-Li_3NbO_4 cell was charged and discharged between 1.0 and 4.8 V with 0.0229 mA cm^{-2} (equivalent to 10 mA g^{-1}) as in the literature.[3] $Li_{1.3}TM_{0.4}Nb_{0.3}O_2$ (TM = Fe, Mn) cells were cycled between 1.5 and 4.8 V with a current density of 0.075–0.089 mA cm^{-2} (equivalent to 20 mA g^{-1}) for the synthesis and air contamination sections. For the electrolyte compatibility study, a lower current was used to ensure that any degradation reactions were not kinetically limited. Therefore, all the $Li_{1.3}Mn_{0.4}Nb_{0.3}O_2$ cells were cycled between 1.5 and 4.8 V with a current density of 0.034–0.036 mA cm^{-2} (equivalent to 10 mA g^{-1}). Both an Arbin BT2000 (Arbin Instruments, USA) and a Neware Battery Test System (Neware Technology Ltd., China) battery cyclers were employed to carry out all the galvanostatic cycling tests.

Additionally, electrochemical impedance spectroscopy (EIS) was performed using a Solartron 1260 impedance analyzer, with an applied AC potential of 10 mV in the frequency range of 1 MHz to 0.1 Hz. The EIS measurements for each electrolyte were performed on the same coin cell in four steps: as assembled,

after a 6 h resting time, after the first charge, and after the first discharge.

Synchrotron XRD

X-ray scattering data was recorded using high-energy X-rays (λ = 0.1666 Å) provided by beamline 28-ID-1 at the National Synchrotron Light Source II (NSLS-II) at Brookhaven National Laboratory. Powders were loaded in amorphous SiO_2 tubes (1.1 mm outer diameter, 1 mm wall thickness, F&D Glass) and placed in the furnace for heating.[25] Temperature was increased up to 960 °C in 20 °C steps in air. Two-dimensional images were recorded in transmission geometry using an amorphous-Si detector, and integrated into one-dimensional XRD patterns using GSAS-II,[26] using LaB_6 (SRM 660c) standards as calibrants.

Results and discussion

Each step of the synthesis process can have a dramatic effect on the electrochemical performances of cathode materials. Fig. 1 highlights three of the parameters that have a major influence on the morphology and phase obtained during the solid-state synthesis of $Li_{1.3}Fe_{0.4}Nb_{0.3}O_2$. These three parameters are: (1) the precursor mixing process, (2) the temperature of the heat-treatment, and (3) the morphology of the precursors used.

Fig. 1a shows the crystal structures of "disordered" and "ordered" rock salt types Li_3NbO_4. Ordered phase consists of four edge-shared NbO_6 octahedra with Li-ion accommodated in a body-centered cubic lattice, while Nb and Li are randomly distributed in the disordered phase.[3,27] The disordered rock salt phase can be electrochemically active when transition metals (TM), such as Fe or Mn, are used to substitute the Li and Nb. However, as shown on Fig. 1b, different precursor mixing techniques can affect the material obtained during the synthesis of cation-disordered rock salt phases. When the precursors are mixed manually, the X-ray diffraction (XRD) pattern acquired after the high-temperature heat treatment (24 hours at 950 °C under air) shows a simple mixture of Li_3NbO_4 (cation-ordered rock salt structure, $I\bar{4}3m$) and $LiFeO_2$ (cation-disordered rock salt, $Fm\bar{3}m$). EDS mapping of this same material also indicates that Nb and Fe are segregated, as different particles are either Nb- or Fe-rich, as shown on Fig. 1c. Fig. S1† presents the morphology and crystal structure of commercially available Nb_2O_5, Fe_2O_3, and Mn_2O_3, which are the common precursors used for the synthesis of $Li_{1.3}TM_{0.4}Nb_{0.3}O_2$ (TM = Fe, Mn).[3,28] All these precursors have micron-sized particles (5–20 μm) and intrinsically high melting points, well beyond typical DRS synthesis temperatures. These characteristics can hinder the diffusion of the transition metals during synthesis, thus preventing the obtention of a pure phase. Contrary to manual grinding, wet ball-milling can provide a significant reduction of the particle size of the reagents, because it is energetic enough to break down metal oxide particles. Consequently, the phase segregation of the final product is alleviated: XRD shows that a pure $Fm\bar{3}m$ phase is obtained with the same synthesis condition after ball milling (Fig. 1b). EDS mapping also confirms a homogeneous distribution of Fe and Nb

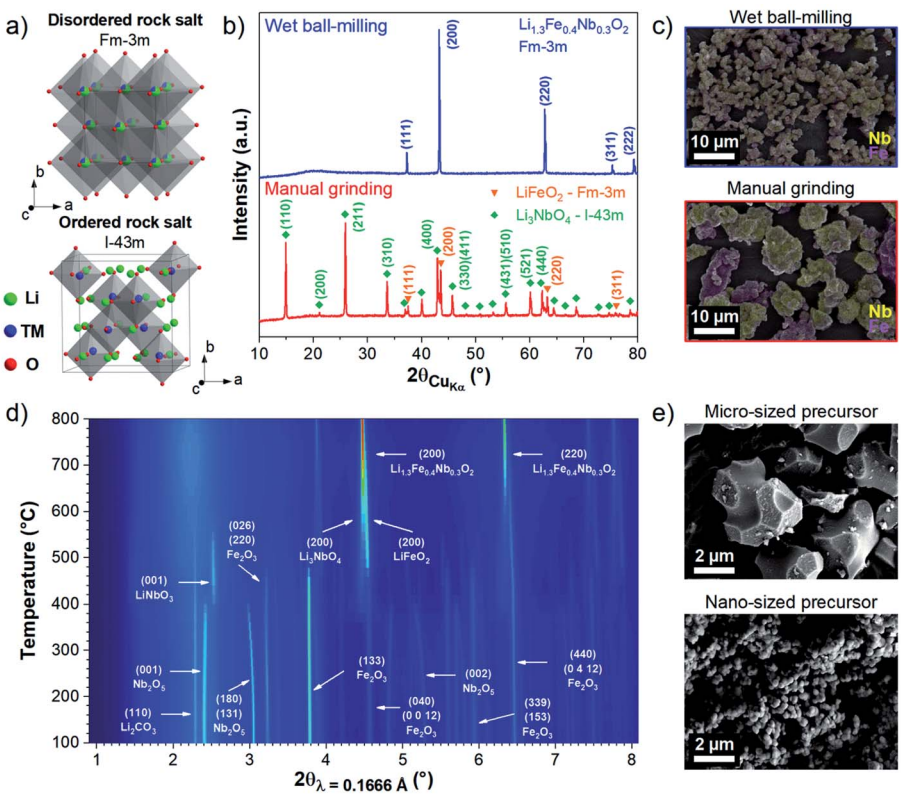

Fig. 1 (a) Crystal structures of disordered and ordered rock salt. Key parameters influencing the morphology and phase obtained during the solid-state synthesis of $Li_{1.3}Fe_{0.4}Nb_{0.3}O_2$: (b and c) precursor mixing process, (d) synthesis temperature, and (e) morphology of the precursors.

in the synthesized product (Fig. 1c). These first results show that an effective mixing of the precursors is mandatory to suppress the segregation of the transition metal phases. Based on these findings, all the subsequent syntheses were performed using wet-ball milling.

The *in situ* heating synchrotron XRD experiment conducted for the synthesis of $Li_{1.3}Fe_{0.4}Nb_{0.3}O_2$ using nano-sized precursors is shown in Fig. 1d. This result gives insight on the range of possible synthesis temperatures, which is another principal synthesis parameter. At lower temperatures, the main peaks of the reagents (Li_2CO_3, Nb_2O_5, and Fe_2O_3) are present, confirming that the wet ball-milling process does not induce any chemical reaction. An intermediate phase, $LiNbO_3$, is formed around 360 °C by the reaction of Li_2CO_3 and Nb_2O_5. As the temperature increases, more Li gets incorporated, generating the cation-disordered rock salt phase Li_3NbO_4 ($Fm\bar{3}m$). In parallel, $LiFeO_2$ ($Fm\bar{3}m$) starts appearing at around 400 °C. By observing the (200) peak of these two DRS phases, it appears that their two different lattices merge into one when the temperature exceeds 760 °C, where the pure $Li_{1.3}Fe_{0.4}Nb_{0.3}O_2$ material is finally obtained. A complementary *ex situ* XRD study with 5 h of dwell time at each temperature (Fig. S3†) shows that this material has a phase stability window of about 200 °C (between 750 and 950 °C). Beyond this point, the temperature induces phase segregation by forming $LiFe_5O_8$ ($P4_332$) and Li_3NbO_4 ($I\bar{4}3m$). It is possible that the continued Li evaporation at high temperature partially leads to the formation of $LiFe_5O_8$ and,[16] without Fe substitution, Nb-rich DRS starts to form Li_3NbO_4 ($I\bar{4}3m$) impurities. This indicates that the synthesis temperature of the material should be chosen carefully: higher temperature generally favors complete phase formation, but can also lead to particle agglomeration, higher cost, and partial Li evaporation.

The last critical parameter, also affecting the phase and the morphology of the synthesized product, is the choice of the precursors. In this study, we used two different sized precursors – nano-sized and micron-sized – and compared the resulting materials using XRD and SEM. It appears that nano-sized precursors promote an effective mixing and allow to obtain a pure phase at only 750 °C. This low synthesis temperature is crucial in order to control the particle morphology, because high temperature inevitably leads to increased grain size of the synthesized product. However, for the micron-sized precursor, a temperature of 950 °C is necessary to obtain a pure phase (Fig. S4†). Thus, the control of the morphology is only possible when using nano-sized precursors as they offer a wider synthesis temperature range. While the particle size of $Li_{1.3}Fe_{0.4}Nb_{0.3}O_2$ is around 4 μm in diameter using micron-sized precursors, 200 nm DRS material can be accomplished using nano-sized precursors (Fig. 1e).

Based on these findings, pure phases of morphology-controlled Li_3NbO_4, $Li_{1.3}Fe_{0.4}Nb_{0.3}O_2$, and $Li_{1.3}Mn_{0.4}Nb_{0.3}O_2$ materials were synthesized using nano-sized metal oxide precursors, as shown in Fig. 2. All the synthesis conditions, including the synthesis of the nano-sized metal oxide precursors, are described in detail in the Experimental methods section. In order to study the effect of the particle morphology on the electrochemical performances of DRS materials, low synthesis temperatures (700 to 750 °C) were used to limit the particle growth. For all three samples, XRD patterns can be indexed with the disordered rock salt structure in the $Fm\bar{3}m$ space group, with no noticeable second phase. The broad peaks at $2\theta_{Mo} \approx 10°$ and $2\theta_{Mo} \approx 26°$ can be attributed to low-intensity superstructure peaks.[29] Interestingly, for the non-substituted material (Li_3NbO_4), the use of nano-sized Nb_2O_5 precursor

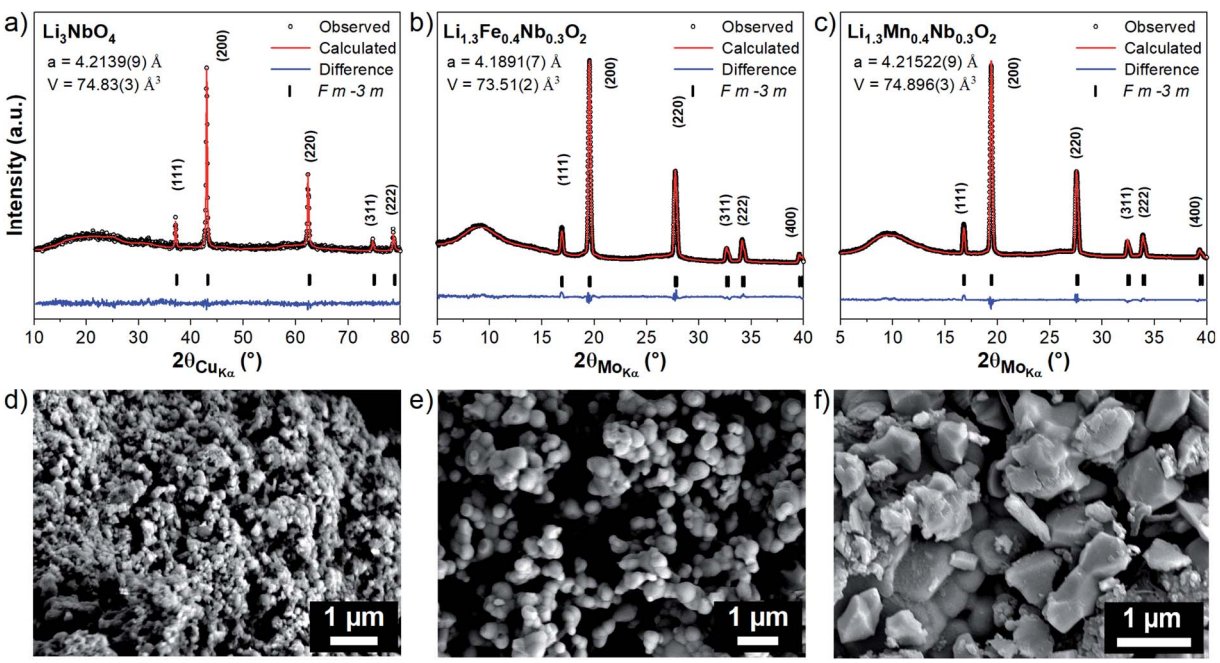

Fig. 2 Rietveld refinements of the XRD patterns and associated SEM images of (a and d) Li_3NbO_4; (b and e) $Li_{1.3}Fe_{0.4}Nb_{0.3}O_2$; and (c and f) $Li_{1.3}Mn_{0.4}Nb_{0.3}O_2$ obtained by using nano-sized precursors.

allows to obtain a single-phase disordered rock salt structure, in contrast with the micron-sized precursor conventionally used. During the synthesis, temperatures above 700 °C are needed for all the Li to diffuse into the structure and form Li_3NbO_4. However, for non-substituted Li_3NbO_4, the disordered rock salt phase transitions to ordered rock salt ($I\bar{4}3m$ space group) occurs at a similar temperature. Thus, only the ordered rock salt structure can be obtained by solid-state reaction with micron-sized precursors (Fig. S5a†) as reported in the literature.[30] However, using nano-sized Nb_2O_5 and LiOH precursor, the disordered rock salt phase is obtained after 1 hour at 700 °C. It appears that the increased surface of contact between the reagents favors a fast and homogeneous diffusion of the Li during the synthesis, making the intermediate $LiNbO_3$ phase only short-lived. For both $Li_{1.3}Fe_{0.4}Nb_{0.3}O_2$ and for $Li_{1.3}Mn_{0.4}Nb_{0.3}O_2$, pure phases are obtained with a 5 hours heat-treatment at 750 °C – compared to 24 hours at 950 °C with micron-sized precursors. Fig. 2d–f shows the resulting morphology of the samples synthesized using these nano-precursors. The particle size of Li_3NbO_4 and $Li_{1.3}Fe_{0.4}Nb_{0.3}O_2$ is limited to 150 nm and 200 nm, respectively, whereas $Li_{1.3}Mn_{0.4}Nb_{0.3}O_2$ particles are around 1 μm. Further efforts were made to reduce the particle size of this last sample by adjusting the temperature and the length of the heat-treatment or the Li source used, but resulted in a non-complete synthesis or impurity formation (Fig. S6†). The morphology of all these samples contrasts from the samples made using micron-sized precursors, presented in Fig. S5,† which show much larger average sizes and wider size distributions.

As reported previously,[3] non-substituted Li_3NbO_4 is not electrochemically active (Fig. S7†). Therefore, we evaluated the electrochemical performances of the Fe- and Mn-substituted materials, at room temperature, in the voltage range of 1.5 to 4.8 V. The voltage profiles of $Li_{1.3}Fe_{0.4}Nb_{0.3}O_2$ and $Li_{1.3}Mn_{0.4}Nb_{0.3}O_2$ are shown in Fig. 3a and c, respectively. Both materials deliver large initial capacities – 312.9 mA h g^{-1} for $Li_{1.3}Fe_{0.4}Nb_{0.3}O_2$ and 339.4 mA h g^{-1} for $Li_{1.3}Mn_{0.4}Nb_{0.3}O_2$ – which indicate that nearly all the lithium was extracted out of the structure. These values are well-beyond the theoretical capacity of $TM^{3+/4+}$ redox couples (118 mA h g^{-1}), as already observed in the literature.[3] Previous studies suggest that,[28,31] in the case of Fe-substituted DRS, small amounts of Fe^{3+} oxidize to Fe^{4+} during the first charge, similar to what has been observed for Li_4FeSbO_6.[32] Then, with further delithiation, oxygen starts to participate in the reaction as Fe^{4+} is reduced back to Fe^{3+}.[28,31] A follow up work is in preparation to assess the origin of the excess capacity in $Li_{1.3}Fe_{0.4}Nb_{0.3}O_2$. Afterward, the material delivers a discharge capacity of 225.8 mA h g^{-1}. Although subsequent cycles result in the decay of the reversible capacity, the extent is significantly reduced in the 750 °C synthesized nanoparticles, compared to the 950 °C synthesized material as shown in Fig. 4. In $Li_{1.3}Mn_{0.4}Nb_{0.3}O_2$, Mn oxidizes from 3+ to 4+ similar to Fe-substituted DRS but keeps a 4+ valence state in the bulk even when the extra capacity is accessed.[28] Previous study, however, reported that repeated oxygen redox leads to significant oxygen loss on the surface, thus causing reduction of surface Mn to 2+.[33]

Although both materials display excess capacities beyond the expected $TM^{3+/4+}$ redox, oxidized oxygen or released oxygen gas

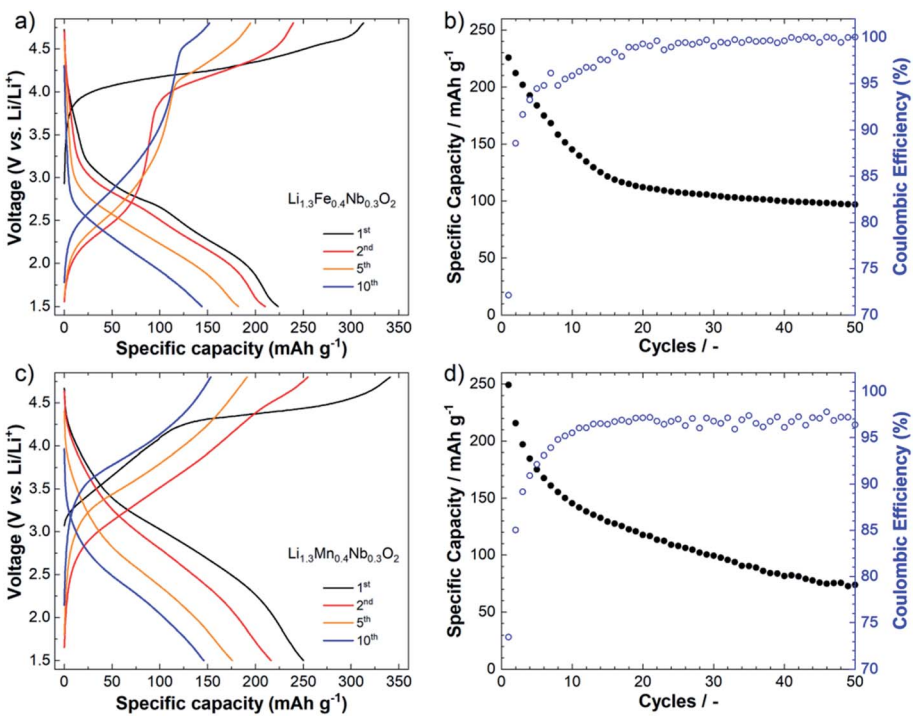

Fig. 3 Voltage profile and cycling stability of morphology-controlled samples of (a and b) $Li_{1.3}Fe_{0.4}Nb_{0.3}O_2$ and (c and d) $Li_{1.3}Mn_{0.4}Nb_{0.3}O_2$ in the voltage range of 1.5–4.8 V *vs.* Li/Li^+ at room temperature.

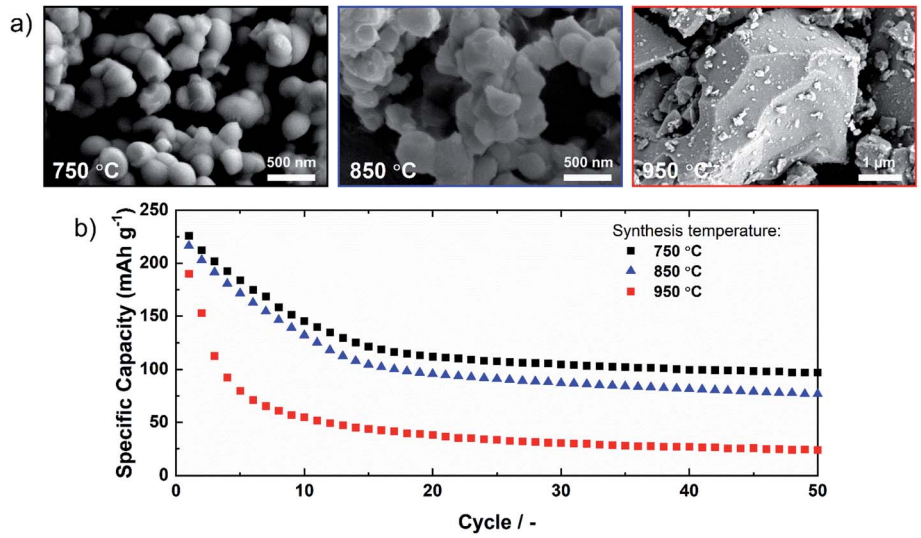

Fig. 4 (a) SEM images and (b) cycling stability of $Li_{1.3}Fe_{0.4}Nb_{0.3}O_2$ synthesized at a temperature of 750 °C (black), 850 °C (blue), and 950 °C (red).

trigger the formation of a surface layer, causing faster capacity decay than traditional TM redox materials.[31,33] Studies on other cathode materials have shown that nanosizing the material can shorten the distance of lithium diffusion and improve its electrochemical performance.[34] However, despite the improved control in morphology, the continued capacity degradation during cycling shows that the DRS system suffers from additional limitations as well. Therefore, we investigated two other factors that are important for practical performance and strongly intertwined with the cathode morphology – (1) the sensitivity of these materials to surface contamination and (2) the electrolyte compatibility.

Ambient-induced surface contamination

It is well-established that impurity species on the surface, caused by the material instability in ambient atmosphere, can have a drastic impact on the performances of the cathode.[35–37] Impurity species formed on the surface of active materials can decrease both electronic and ionic conductivities while also consuming part of the active lithium.[38] Nanoparticles, with large surface area, typically have enhanced sensitivity to surface chemistry. Thus, the synthesized nanoparticles were utilized here to help understand how sample handling and storage can affect the DRS material's properties. In this experiment, pristine cathode powders of morphology-controlled $Li_{1.3}Fe_{0.4}Nb_{0.3}O_2$ and $Li_{1.3}Mn_{0.4}Nb_{0.3}O_2$ were split into three different vials each and exposed to the following conditions: one vial was sealed and stored in an Ar-filled glovebox (pristine); the second vial was left open under a continuous air flow for 4 weeks (air-exposed); the third sample was prepared by heat-treating the air-exposed sample at 500 °C for 2 h under air for $Li_{1.3}Fe_{0.4}Nb_{0.3}O_2$, and under Ar for $Li_{1.3}Mn_{0.4}Nb_{0.3}O_2$ (regenerated). This heat-treatment temperature was selected based on a previous study of the surface contamination of high Ni layered oxide,[35] and then confirmed by the TGA measurements.

Fig. 5 shows the TGA, electrochemical performances, XRD, and XPS of pristine, air-exposed, and regenerated $Li_{1.3}Fe_{0.4}Nb_{0.3}O_2$ nanoparticles. For the thermogravimetric analysis, presented in Fig. 5a, all three samples were heated to 750 °C with isothermal segments at 150, 350, and 500 °C, as detailed in the Experimental methods part. These segments were designed to ensure the complete removal of surface species such as H_2O, $LiHCO_3$, LiOH, and Li_2CO_3, as these evaporate or decompose at temperatures comprised between 100 and 710 °C.[35] The pristine $Li_{1.3}Fe_{0.4}Nb_{0.3}O_2$ material shows negligible weight loss compared with the alumina reference (Fig. S8†), indicating that minimal amount of surface species is present in the sample after the synthesis. On the other hand, the mass loss of the air-exposed sample exceeds 4%, suggesting that a severe reaction takes place with the ambient atmosphere. A large part of the weight loss corresponds to $LiHCO_3$ and LiOH, similar to observations on air-exposed $LiNi_{0.85}Co_{0.10}Al_{0.05}O_2$ or $LiNi_{0.8}Co_{0.1}Mn_{0.1}O_2$.[35,39] These results also show that the majority of the impurities can be removed by annealing at 500 °C. Consequently, we investigated the possibility of regenerating the air-exposed sample using a heat-treatment at this temperature.

Electrochemical performance of all three samples are presented in Fig. 5b and c. After the pristine material has been exposed to air, the first discharge is significantly reduced, from 225.8 mA h g^{-1} to 188.5 mA h g^{-1}. This is accompanied by a drastic increase in the polarization of the cell from 80 mV to 650 mV. The regeneration of the sample reduces this polarization and the first discharge capacity is improved, reaching 210.0 mA h g^{-1}. X-ray diffraction and XPS were additionally conducted to compare in detail the structure and surface chemistry of the three samples and understand the origin of the difference in electrochemical performance.

Fig. 5d presents the XRD pattern of air-exposed and regenerated samples. The diffraction pattern of the air-exposed sample confirms the presence of impurity peaks which were

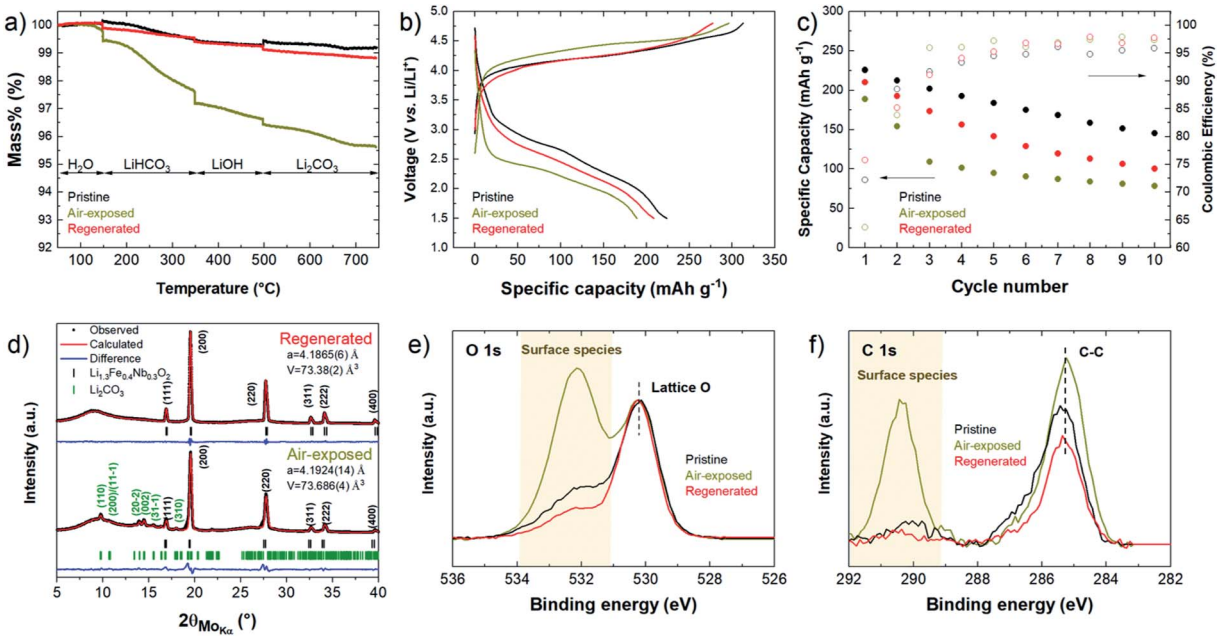

Fig. 5 Study of the effect of surface contamination on the morphology-controlled sample of $Li_{1.3}Fe_{0.4}Nb_{0.3}O_2$ in pristine state, after 4 weeks of air exposure, and after regeneration by heat treatment: (a) thermogravimetric analysis, (b) first voltage profiles, (c) cycling stability, (d) profile matching refinement of the XRD patterns, and XPS measurements of the (e) O 1s and (f) C 1s core regions.

not present in the pristine sample (shown in Fig. 2b). These peaks can be indexed as lithium carbonate with the *C*2/*c* space group. This observation contrasts with most conventional cathode materials, where the impurities formed during air exposure can usually not be detected by XRD, because they are present in limited amounts and in an amorphous state.[35,40] Furthermore, the main diffraction peaks of the phase exhibit a widening at a lower angle (Fig. S9†). This can indicate the formation of other DRS phases, such as FeO, with larger lattice parameters. It is however difficult to determine with certainty the nature of this second impurity as it shares the same space group as the cathode material. All the impurity peaks disappeared by annealing the air-exposed sample at 500 °C. The cell parameters of all three samples are similar – 4.1891(7) Å for the pristine, 4.1924(14) Å for the air-exposed, and 4.1865(6) Å for the regenerated sample – indicating that the reactivity of the material with air does not affect the bulk structure.

Surface-sensitive XPS measurements, presented in Fig. 5e and f, clearly show how air-exposure and regeneration affect the cation-disordered rock salt surface chemistry. The O 1s spectra were normalized with respect to the intensity of the peak at 530.2 eV, indexed to $Li_{1.3}Fe_{0.4}Nb_{0.3}O_2$ lattice oxygen. These results show that, relative to lattice oxygen, a higher binding energy peak around 532.7 eV significantly increases in intensity after air exposure, and then decreases even below the level of the pristine sample after regeneration. This broad peak for the air-exposed sample arises from a combination of Li_2CO_3/$LiHCO_3$ (≈532.0–532.5 eV) and LiOH (≈531.2 eV) at the surface. Complementary measurements of the C 1s core region further support this assignment, with the air-exposed sample showing a strong peak centered at 290.0 eV that is consistent with Li_2CO_3 (or $LiHCO_3$) formation.[40] This peak is again significantly reduced in the regenerated sample in agreement with the trend observed in the O 1s core region. When approximating the surface oxygen species as a continuous surface layer,[41] the layer thickness can be estimated as 0.46, 1.24, and 0.32 nm for pristine, air-exposed, and regenerated samples, respectively. In conclusion, although small amount of surface species, such as LiOH and Li_2CO_3, develop during the synthesis of $Li_{1.3}Fe_{0.4}Nb_{0.3}O_2$, the amount significantly increases during the storage in ambient air. Post-annealing mostly decomposes the surface species developed during the synthesis and storage, resulting in the thinnest surface overlayer. As can be seen on the cycling data (Fig. 5a and b), the original capacity and cycling retention are not fully recovered, however, suggesting a loss of active material due to the formation of the surface species during air exposure. While Li_2CO_3 is decomposed during the heat treatment, as confirmed by the XPS results, some of the other impurities formed are challenging to probe as they can present similar structures (such as FeO[42,43]) and/or oxidation state than the cathode itself.

A similar study was performed on the nanoparticles of $Li_{1.3}Mn_{0.4}Nb_{0.3}O_2$ and the results are presented in the ESI (Fig. S10).† In this case, Li_2CO_3 was only detected as a trace amount on the diffraction pattern, which can be explained by the smaller surface area of this material compared to the Fe-substituted sample. The TGA and XPS results nevertheless demonstrate a larger amount of impurities, suggesting the presence of amorphous phases at the surface of the cathode. This is also confirmed by the drastic degradation of the capacity of the material. The first discharge capacity of the air-exposed sample was only 167.8 mA h g^{-1} compared to 253.3 mA h g^{-1}

for pristine sample. Crystalline lithium carbonate is not detected anymore by XRD after heat-treatment of the air-exposed sample, and the TGA shows a large reduction of the amount of impurities. The mass loss when the temperature exceeds 700 °C nevertheless indicates that some impurities might still be present after regeneration. This result is also consistent with significant surface species still observed in XPS for regenerated sample despite the amount being reduced from the air-exposed sample. As a result, the voltage profile of the regenerated sample does not show a major improvement compared to the air-exposed sample indicating that air exposure is more detrimental to the Mn-substituted material than its Fe counterpart.

Electrolyte compatibility

Cathode–electrolyte interphase (CEI) layer plays an essential role in determining the electrochemical performance of Li-ion batteries.[22,44] While a well-functioning interphase layer will passivate the electrolyte/electrode interphase and prevent further degradation of the material without hindering Li-ion diffusion, an unstable surface layer that fails to passivate the surface can result in the consequential breakdown of the active material. Despite its importance, detailed study on the formation and evolution of this interphase is still limited, as it depends on a lot of factors such as the cathode material's crystal structure, chemical constitution, and operating voltage as well as the choice of electrolyte.[17]

Most previous studies on DRS cathodes were performed with standard carbonate-based electrolyte, which has been best engineered for conventional cathode materials operating at voltages lower than 4.5 V. Unfortunately, anionic redox cathode materials, including Li-excess layered oxides and DRS materials, rely on a high voltage cut-off ($\approx$4.8 V) to achieve high capacity. Moreover, oxidized oxygen or released oxygen gas can further trigger reactions with the electrolyte and form a surface layer.[22] These reactions can be even more exacerbated by high surface area cathode materials such as nanoparticles.

Herein, we investigated two additional advanced electrolytes to understand the interphase formed by the electrolytes with disordered rock salt cathode materials. $Li_{1.3}Mn_{0.4}Nb_{0.3}O_2$ (Mn-DRS) material was used for this study in order to compare with another Mn-based Li-excess anionic redox material, Li$[Li_{0.144}Ni_{0.136}Co_{0.136}Mn_{0.544}]O_2$ (LR-NMC), which has been more widely studied. Micron-sized samples were used to reduce possible surface contamination, for instance, during the transfer to the glovebox. The three different electrolyte systems studied are: (1) baseline electrolyte: 1 M lithium hexafluorophosphate ($LiPF_6$) in a 3 : 7 volume mixture of ethylene carbonate (EC) and dimethyl carbonate (DMC); (2) LiDFOB electrolyte: 1 M $LiPF_6$ in a 3 : 7 volume mixture of EC and DMC with 2 wt% lithium difluoro(oxalate)borate (LiDFOB) as an additive; and (3) FEC electrolyte: 1 M $LiPF_6$ in a 1 : 4 volume mixture of fluoroethylene carbonate (FEC) and DMC.

Fig. 6a and b presents the cycling stability of LR-NMC and Mn-DRS cells made with three different electrolytes. As shown, the choice of electrolytes significantly impacts the cycling stability of Mn-DRS contrary to what is observed for LR-NMC. Indeed, for Mn-DRS, the first discharge capacity for LiDFOB only reaches 240 mA h g^{-1}, whereas the baseline and FEC electrolytes are higher, around 288 mA h g^{-1} and 278 mA h g^{-1}, respectively. FEC electrolyte cell, nevertheless, exhibits a faster capacity decay than the two other cells, its discharge capacity being only 85 mA h g^{-1} after only 10 cycles, compared to 168 mA h g^{-1} for the baseline and 115 mA h g^{-1} for LiDFOB electrolyte. Even after the first few formation cycles, the coulombic efficiencies of all these cells are between 90 and 97% implying that severe side reactions continue to occur during cycling. The low coulombic efficiencies can come from different factors, such as electrolyte decomposition,[45] surface species decomposition,[36,46] and gassing.[31,47] For disordered rock salt materials, O_2 gas generation has been shown in the literature to occur mainly during the first cycle, while CO_2 gas generation can also happen during further cycles.[47]

XPS was carried out to understand the changes in chemical composition of the CEI layer with the choice of cathode materials and electrolytes. Fig. 6c–e compares the O 1s, Li 1s–Mn 3p, and P 2p core regions of the pristine and cycled LR-NMC and Mn-DRS electrodes, tested with three different electrolytes. Peak fits of each spectra are presented to indicate the dependence of specific CEI species on the electrolyte used, with approximate peak assignments detailed in Table S1.† These assignments are based on a range of previous CEI studies on oxide cathodes.[48–50] The C–C carbon black peak at 284.8 eV was used to calibrate the Li-rich NMC samples, while the Nb 3d peak associated with the Nb^{5+} environment was used for $Li_{1.3}Mn_{0.4}Nb_{0.3}O_2$. This second calibration method was selected due to differential charging effects that resulted in large relative binding energy shifts between $Li_{1.3}Mn_{0.4}Nb_{0.3}O_2$ and other cathode components (PVDF binder and carbon black). This effect can occur when measuring samples composed of mixed conducting and insulating materials,[51,52] and is more prevalent for the electronically insulating $Li_{1.3}Mn_{0.4}Nb_{0.3}O_2$ compound. For PVDF and carbon black, this effect results in over a 0.5 eV variation in their peak positions relative to the $Li_{1.3}Mn_{0.4}Nb_{0.3}O_2$ Nb 3d lattice peak (Fig. S11†). As detailed later, this effect can also cause shifts in the relative positions of insulating CEI species, including LiF.

Focusing first on the pristine compounds, there is a significant Li_2CO_3 layer on the surface of the Mn-DRS even before cycling, based on the strong peaks at 532.3 eV in the O 1s region and at 55.6 eV in the Li 1s region. As discussed in an earlier section, Li_2CO_3 surface impurity can come from residual precursors, or reactions between CO_2 in the atmosphere and the active cathode powder,[38] but the latter is more likely in Mn-DRS case, since the high-temperature heat-treatment (950 °C for 24 h) was conducted in Ar atmosphere during the synthesis. Despite the care taken to minimize atmospheric exposure during the experiments, high chemical sensitivity with ambient air for Mn-DRS leads to a surface layer more than 6 times thicker (3.3 nm) than the LR-NMC counterpart (0.49 nm). For both materials, this initial surface Li_2CO_3 layer breaks down at high state of charge (Fig. S12†), consistent with previously reported work.[36] Reductions of surface layer during charge are observed across all three electrolytes in Mn-DRS cathode as summarized in Fig. S12a.†

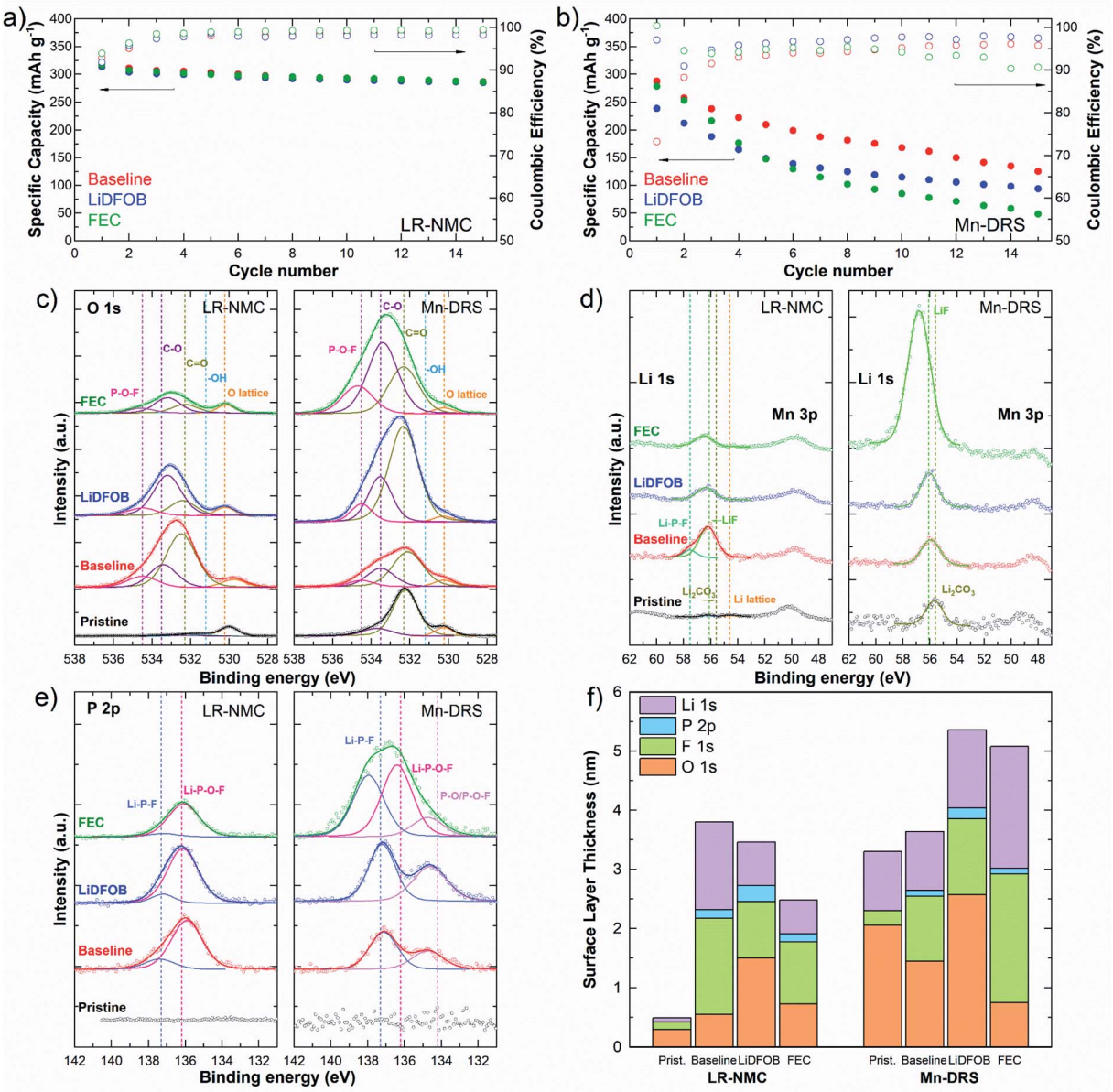

Fig. 6 Cycling stability of (a) $Li[Li_{0.144}Ni_{0.136}Co_{0.136}Mn_{0.544}]O_2$ (LR-NMC) and (b) $Li_{1.3}Mn_{0.4}Nb_{0.3}O_2$ (Mn-DRS) with the 3 different electrolytes studied. XPS spectra of the (c) O 1s, (d) Li 1s–Mn 3p, and (e) P 2p region of LR-NMC and Mn-DRS in the pristine state and after first discharge for the 3 electrolytes tested. (f) Surface layer thickness calculated from the XPS spectra with elemental contribution.

In the discharged state, new peaks arise as a thicker CEI develops for both cathode materials. In the O 1s core region, the single peak found at 530.2 eV is indexed to the lattice oxygen (TM–O). Higher energy peaks at 531–536 eV are commonly attributed to the surface CEI species,[48–50] therefore, their relative intensities against the lattice oxygen are a good indicator to estimate CEI thickness. In Fig. 6f, the elemental composition of the CEI (Li, P, F, and O) for each sample was normalized to the estimated CEI thickness. Although Mn-DRS initially starts with a thicker surface layer, a similar CEI thickness is found in LR-NMC by the end of the first cycle when using the baseline electrolyte. However, when LiDFOB additive or FEC : DMC co-solvent electrolytes are used, the two material systems show diverging trends in both CEI thickness and composition. In the case of LR-NMC, the overall intensities for CEI components get reduced compared to the baseline electrolyte, while the peak locations in O 1s, P 2p, and Li 1s remain mostly consistent. This indicates that the overall CEI thickness was reduced for LiDFOB and FEC electrolytes without significant changes in their chemical composition.

On the other hand, for Mn-DRS material, CEI thickness increases from 3.64 nm for baseline to 5.36 nm for LiDFOB and 5.08 nm for FEC electrolytes. In both electrolytes, the O 1s signal is dominated by a broad peak at a higher binding energy than lattice TM–O (≈530.2 eV), which comprised of several oxygen-containing groups, such as C–O (≈533.5 eV), C=O (≈532.3

eV), O–H (≈531.2 eV), and P–O–F (≈534.4 eV) species. As the cycled electrodes were washed with DMC before XPS measurement, we assume that no Li-salt remained on the electrode. As a result, the relative amounts of detected Li, P, and F components can be correlated to the CEI species developed through the Li salt ($LiPF_6$) degradation in the electrolyte that leads to the formation of LiF and $Li_xPF_yO_z$ and other species.[48–50] As summarized in the elemental composition in Fig. 6f, Mn-DRS had consistently larger contributions of Li and F species for all 3 electrolytes than the LR-NMC cathode. The difference between these two systems becomes increasingly wider from baseline, LiDFOB, to FEC electrolyte, as both LiDFOB and FEC electrolytes show more salt decomposition in Mn-DRS, while it was found to be suppressed in LR-NMC.[18,53]

Particularly, in the FEC electrolyte with Mn-DRS, sharp peaks at ≈56.8 eV in the Li 1s region (Fig. 6d) and at ≈686.6 eV in the F 1s region (Fig. S13b†) were detected compared to baseline or LiDFOB electrolytes. These peaks were attributed to LiF in spite of its ≈0.7 eV higher binding energy shift relative to the reference material in both the Li and F 1s spectra. This shift may be a result of the more insulating nature of LiF and the large quantity of these species found for the FEC electrolyte with Mn-DRS. Additionally, high intensity peaks associated with Li–P–F and Li–P–O–F species in the P 2p region were detected, which also arise from Li-salt decomposition. The pronounced increase in highly ionically resistive LiF at the CEI for the FEC electrolyte Mn-DRS electrode is consistent with the growth in impedance,[54] as observed in Fig. S14.† Although the LiDFOB electrolyte exhibited the thickest CEI of all six cycled electrodes based on our thickness estimation method, this is likely a result of the high content of C=O and C–O species detected in the O 1s region. Indeed, less salt decomposition components were observed with the LiDFOB electrolyte, suggesting that solvent molecules are mainly involved in the CEI formation process. These results show that the choice of the electrolyte is crucial to enable long cycling stability of cation-disordered rock salt materials. Even compared with the similar Mn-based Li-excess anionic redox cathode material, DRS material forms distinct interphase species with the 3 electrolytes used for this study.

Based on this study of the electrolyte compatibility, where significant side reactions of the electrolyte components (and particularly the $LiPF_6$ salt) with Mn-DRS have been observed, the cycling stability of cation disordered rock salt cathodes could be further improved by different strategies. First, implementing highly concentrated electrolyte with alternative Li-salt, such as lithium bis(fluorosulfonyl)imide (LiFSI), could be beneficial, as the higher stability of LiFSI toward hydrolysis, in conjunction with a lower interfacial resistance, can improve the cycling stability.[55,56] Alternatively, surface modification, such as Al_2O_3 coating with atomic layer deposition (ALD) method, can help suppressing the undesirable side reactions between the active material and electrolyte components.[57]

Conclusion

A systematic study of the solid-state synthesis of cation disordered rock salt materials was carried out, in which the influence of important synthesis parameters, such as precursor mixing, synthesis temperature, and precursor choice, on the final product was investigated. Three different morphology-controlled DRS materials, Li_3NbO_4, $Li_{1.3}Fe_{0.4}Nb_{0.3}O_2$, and $Li_{1.3}Mn_{0.4}Nb_{0.3}O_2$ were synthetized at low temperature using nano-sized precursors. This method allowed to obtain particle sizes comprised between 150 nm and 1 μm, contrasting with the several micrometers-sized particles obtained with a standard high-temperature solid-state synthesis. Whereas the initial discharge capacity of the substituted samples reaches reported values in the literature and the capacity retention is improved, this class of material still suffers from poor cyclability. In order to investigate this issue, two possible limitations of this system were evaluated: surface contamination from air exposure and electrolyte stability. It appears that both $Li_{1.3}Fe_{0.4}Nb_{0.3}O_2$ and $Li_{1.3}Mn_{0.4}Nb_{0.3}O_2$ are highly sensitive to air exposure, as evidenced by TGA, XRD and XPS results. A heat-treatment at 500 °C allows the removal of most surface species, reducing the polarization of the cell and inducing the partial recovery of the lost capacity. Nevertheless, inert atmosphere storage after synthesis is still highly recommended for cation-disordered rock salt materials. For the electrolyte compatibility study, LiDFOB additives or FEC : DMC co-solvent electrolyte, although suitable for other oxygen redox material such as Li-excess NMC, were shown to lead to a thick CEI when used with Mn-substituted DRS cathode. This process occurs starting from the first discharge and results in a rapid increase of the cell impedance, hindering the cycling stability of the cathode. Therefore, evaluating the electrochemical compatibility of the electrolyte with the DRS cathode is critical for this new class of materials to enhance their electrochemical performances.

Author contributions

H. C., J.-M. D., and Y. S. M. conceived the ideas and planned the experiments. H. C., C. M., B. S., R. H., and Y. L. carried out the synthesis and electrochemical work; H. C. and B. S. collected XPS data that was analyzed with the help of Z. L.-H. and L. F. J. P.; H. C., A. G., G. E. K., and K. W. C. collected and analyzed *in situ* temperature-XRD data; H. C., J.-M. D., B. S., and Z. L.-H. wrote the manuscript. The manuscript was revised with the help of all authors.

Conflicts of interest

There are no conflicts of interest to declare.

Acknowledgements

This work is supported by the NorthEast Center for Chemical Energy Storage (NECCES), an Energy Frontier Research Center funded by the U.S. Department of Energy, Office of Science, Basic Energy Sciences under Award No. DE-SC0012583. The authors would like to acknowledge the UCSD Crystallography Facility. This work was performed in part at the San Diego Nanotechnology Infrastructure (SDNI) of UCSD, a member of the National Nanotechnology Coordinated Infrastructure,

which is supported by the National Science Foundation (Grant ECCS-1542148). Characterization work was performed in part at the UC Irvine Materials Research Institute (IMRI) using instrumentation funded in part by the National Science Foundation Major Research Instrumentation Program under Grant No. CHE-1338173, as well as Lawrence Livermore National Laboratory under Contract DE-AC52-07NA27344, release number LLNL-JRNL-786041. Work done at Brookhaven used beamline 28-ID-1 of the National Synchrotron Light Source II, a U.S. Department of Energy (DOE) Office of Science User Facility operated for the DOE Office of Science by Brookhaven National Laboratory under contract No. DE-SC0012704. We would like to acknowledge Neware for the generous donation of BTS4000 cyclers. We also thank M. Zhang, H. Nguyen, W. Li, M. Jones, P. Reeves, C. P. Grey, and M. S. Whittingham for their insightful discussions.

References

1 S. Hy, H. Liu, M. Zhang, D. Qian, B. J. Hwang and Y. S. Meng, *Energy Environ. Sci.*, 2016, **9**, 1931–1954.
2 P. K. Nayak, E. M. Erickson, F. Schipper, T. R. Penki, N. Munichandraiah, P. Adelhelm, H. Sclar, F. Amalraj, B. Markovsky and D. Aurbach, *Adv. Energy Mater.*, 2017, **8**, 1702397.
3 N. Yabuuchi, M. Takeuchi, M. Nakayama, H. Shiiba, M. Ogawa, K. Nakayama, T. Ohta, D. Endo, T. Ozaki, T. Inamasu, K. Sato and S. Komaba, *Proc. Natl. Acad. Sci. U. S. A.*, 2015, **112**, 7650–7655.
4 D. A. Kitchaev, Z. Lun, W. D. Richards, H. Ji, R. J. Clément, M. Balasubramanian, D. H. Kwon, K. Dai, J. K. Papp, T. Lei, B. D. McCloskey, W. Yang, J. Lee and G. Ceder, *Energy Environ. Sci.*, 2018, **11**, 2159–2171.
5 J. Lee, A. Urban, X. Li, D. Su, G. Hautier and G. Ceder, *Science*, 2014, **343**, 519–522.
6 N. Yabuuchi, *Chem. Lett.*, 2017, **46**, 412–422.
7 A. Urban, J. Lee and G. Ceder, *Adv. Energy Mater.*, 2014, **4**, 1400478.
8 J. Lee, J. K. Papp, R. J. Clément, S. Sallis, D. H. Kwon, T. Shi, W. Yang, B. D. McCloskey and G. Ceder, *Nat. Commun.*, 2017, **8**, 1–10.
9 R. J. Clément, Z. Lun and G. Ceder, *Energy Environ. Sci.*, 2020, **13**, 345–373.
10 N. Yabuuchi, M. Takeuchi, S. Komaba, S. Ichikawa, T. Ozaki and T. Inamasu, *Chem. Commun.*, 2016, **52**, 2051–2054.
11 R. Wang, X. Li, L. Liu, J. Lee, D. Seo, S. Bo, A. Urban and G. Ceder, *Electrochem. Commun.*, 2015, **60**, 70–73.
12 X. Fan, Q. Qin, D. Liu, A. Dou, M. Su, Y. Liu and J. Pan, *J. Alloys Compd.*, 2019, **797**, 961–969.
13 R. Chen, S. Ren, M. Knapp, D. Wang, R. Witter, M. Fichtner and H. Hahn, *Adv. Energy Mater.*, 2015, **5**, 1401814.
14 M. Freire, N. V. Kosova, C. Jordy, D. Chateigner, O. I. Lebedev, A. Maignan and V. Pralong, *Nat. Mater.*, 2015, **15**, 173–177.
15 J. Lee, D. A. Kitchaev, D.-H. Kwon, C.-W. Lee, J. K. Papp, Y.-S. Liu, Z. Lun, R. J. Clément, T. Shi, B. D. McCloskey, J. Guo, M. Balasubramanian and G. Ceder, *Nature*, 2018, **556**, 185–190.
16 E. N. Lysenko, A. P. Surzhikov, E. V. Nikolaev and V. A. Vlasov, *J. Therm. Anal. Calorim.*, 2018, **134**, 81–87.
17 H. Zhao, X. Yu, J. Li, B. Li, H. Shao, L. Li and Y. Deng, *J. Mater. Chem. A*, 2019, **7**, 8700–8722.
18 J. Cha, J. Han, J. Hwang, J. Cho and N. Choi, *J. Power Sources*, 2017, **357**, 97–106.
19 B. Qiu, M. Zhang, L. Wu, J. Wang, Y. Xia, D. Qian, H. Liu, S. Hy, Y. Chen, K. An, Y. Zhu, Z. Liu and Y. S. Meng, *Nat. Commun.*, 2016, **7**, 12108.
20 J. Rodríguez-Carvajal, *Phys. B*, 1993, **192**, 55–69.
21 N. Schulz, R. Hausbrand, C. Wittich, L. Dimesso and W. Jaegermann, *J. Electrochem. Soc.*, 2018, **165**, A833–A846.
22 Q. Li, Y. Wang, X. Wang, X. Sun, J. N. Zhang, X. Yu and H. Li, *ACS Appl. Mater. Interfaces*, 2020, **12**, 2319–2326.
23 P. Niehoff and M. Winter, *Langmuir*, 2013, **29**, 15813–15821.
24 D. R. Baer and M. H. Engelhard, *J. Electron Spectrosc. Relat. Phenom.*, 2010, **178–179**, 415–432.
25 P. J. Chupas, K. W. Chapman, C. Kurtz, J. C. Hanson, P. L. Lee and C. P. Grey, *J. Appl. Crystallogr.*, 2008, **41**, 822–824.
26 B. H. Toby and R. B. Von Dreele, *J. Appl. Crystallogr.*, 2013, **46**, 544–549.
27 Q. Jacquet, A. Perez, D. Batuk, G. Van Tendeloo, G. Rousse and J. M. Tarascon, *Chem. Mater.*, 2017, **29**, 5331–5343.
28 N. Yabuuchi, M. Nakayama, M. Takeuchi, S. Komaba, Y. Hashimoto, T. Mukai, H. Shiiba, K. Sato, Y. Kobayashi, A. Nakao, M. Yonemura, K. Yamanaka, K. Mitsuhara and T. Ohta, *Nat. Commun.*, 2016, **7**, 13814.
29 M. A. Jones, P. J. Reeves, I. D. Seymour, M. Cliffe, S. E. Dutton and C. P. Grey, *Chem. Commun.*, 2019, **55**, 9027–9030.
30 D. R. Modeshia, R. Walton, M. Mitchel and S. Ashbrook, *Dalton Trans.*, 2010, **39**, 5949–5964.
31 M. Luo, S. Zheng, J. Wu, K. Zhou, W. Zuo, M. Feng, H. He, R. Liu, J. Zhu, G. Zhao, S. Chen, W. Yang, Z. Peng, Q. Wu and Y. Yang, *J. Mater. Chem. A*, 2020, **8**, 5115–5127.
32 E. McCalla, M. T. Sougrati, G. Rousse, E. J. Berg, A. Abakumov, N. Recham, K. Ramesha, M. Sathiya, R. Dominko, G. Van Tendeloo, P. Novák and J. M. Tarascon, *J. Am. Chem. Soc.*, 2015, **137**, 4804–4814.
33 D. Chen, W. H. Kan and G. Chen, *Adv. Energy Mater.*, 2019, **9**, 1901255.
34 C. Siu, I. D. Seymour, S. Britto, H. Zhang, J. Rana, J. Feng, F. O. Omenya, H. Zhou, N. A. Chernova, G. Zhou, C. P. Grey, L. F. J. Piper and M. S. Whittingham, *Chem. Commun.*, 2018, **54**, 7802–7805.
35 N. V. Faenza, L. Bruce, Z. W. Lebens-Higgins, I. Plitz, N. Pereira, L. F. J. Piper and G. G. Amatucci, *J. Electrochem. Soc.*, 2017, **164**, A3727–A3741.
36 S. E. Renfrew and B. D. McCloskey, *J. Am. Chem. Soc.*, 2017, **139**, 17853–17860.
37 Y. You, H. Celio, J. Li, A. Dolocan and A. Manthiram, *Angew. Chem.*, 2018, **57**, 6480–6485.
38 O. Haik, N. Leifer, Z. Samuk-Fromovich, E. Zinigrad, B. Markovsky, L. Larush, Y. Goffer, G. Goobes and D. Aurbach, *J. Electrochem. Soc.*, 2010, **157**, A1099–A1107.

39 J. Sicklinger, M. Metzger, H. Beyer, D. Pritzl and H. A. Gasteiger, *J. Electrochem. Soc.*, 2019, **166**, A2322–A2335.

40 A. Grenier, H. Liu, Z. W. Lebens-Higgins, L. F. J. Piper, O. J. Borkiewicz, K. M. Wiaderek, P. J. Chupas and K. W. Chapman, *Chem. Mater.*, 2017, **29**, 7345–7352.

41 M. P. Seah, *Surf. Interface Anal.*, 1980, **2**, 222–239.

42 R. Dutta, S. J. Tracy, C. V. Stan, V. B. Prakapenka, R. J. Cava and T. S. Duffy, *Phys. Chem. Miner.*, 2018, **45**, 367–379.

43 O. Crisan and A. D. Crisan, *J. Alloys Compd.*, 2011, **509**, 6522–6527.

44 I. Takahashi, H. Kiuchi, A. Ohma, T. Fukunaga and E. Matsubara, *J. Phys. Chem. C*, 2020, **124**, 9243–9248.

45 S. E. Renfrew and B. D. McCloskey, *ACS Appl. Energy Mater.*, 2019, **2**, 3762–3772.

46 N. Mahne, S. E. Renfrew, B. D. McCloskey and S. A. Freunberger, *Angew. Chem., Int. Ed.*, 2018, **57**, 5529–5533.

47 M. J. Crafton, Y. Yue, T. Y. Huang, W. Tong and B. D. McCloskey, *Adv. Energy Mater.*, 2020, **10**, 2001500.

48 Y. Lu, A. N. Mansour, N. Yabuuchi and Y. Shao-horn, *Chem. Mater.*, 2009, **21**, 4408–4424.

49 L. Baggetto, N. J. Dudney and G. M. Veith, *Electrochim. Acta*, 2013, **90**, 135–147.

50 Z. W. Lebens-Higgins, N. V. Faenza, M. D. Radin, H. Liu, S. Sallis, J. Rana, J. Vinckeviciute, P. J. Reeves, M. J. Zuba, F. Badway, N. Pereira, K. W. Chapman, T. L. Lee, T. Wu, C. P. Grey, B. C. Melot, A. Van Der Ven, G. G. Amatucci, W. Yang and L. F. J. Piper, *Mater. Horiz.*, 2019, **6**, 2112–2123.

51 L. Dahéron, R. Dedryvère, H. Martinez, M. Ménétrier, C. Denage, C. Delmas and D. Gonbeau, *Chem. Mater.*, 2008, **20**, 583–590.

52 L. W. Wangoh, Y. Huang, R. L. Jezorek, A. B. Kehoe, G. W. Watson, F. Omenya, N. F. Quackenbush, N. A. Chernova, M. S. Whittingham and L. F. J. Piper, *ACS Appl. Mater. Interfaces*, 2016, **8**, 11532–11538.

53 Y. Qian, P. Niehoff, M. Börner, M. Grützke, X. Mönnighoff, P. Behrends, S. Nowak, M. Winter and F. M. Schappacher, *J. Power Sources*, 2016, **329**, 31–40.

54 M. Gauthier, T. J. Carney, A. Grimaud, L. Giordano, N. Pour, H. Chang, D. P. Fenning, S. F. Lux, O. Paschos, C. Bauer, F. Maglia, S. Lupart, P. Lamp and Y. Shao-horn, *J. Phys. Chem. Lett.*, 2015, **6**, 4653–4672.

55 Y. Yamada, J. Wang, S. Ko, E. Watanabe and A. Yamada, *Nat. Energy*, 2019, **4**, 269–280.

56 M. A. Cambaz, B. P. Vinayan, H. Euchner, S. A. Pervez, H. Geßwein, T. Braun, A. Gross and M. Fichtner, *ACS Appl. Mater. Interfaces*, 2019, **11**, 39848–39858.

57 B. Huang, R. Wang, Y. Gong, B. He and H. Wang, *Front. Chem.*, 2019, **7**, 107.

